

3GPP-Like GBSM THz Channel Modeling for Indoor Office and Urban Microcellular Scenarios

Zhaowei Chang, Jianhua Zhang, Pan Tang, Lei Tian, Hao Jiang, Ximan Liu, and Guangyi Liu

Abstract—Terahertz (THz) communication is envisioned as one of the possible technologies for the sixth-generation (6G) communication system due to its rich spectrum. To evaluate the performance of THz communication, it is essential to propose THz channel models within the common framework of the geometry-based stochastic model (GBSM) in the 3rd Generation Partnership Project (3GPP). This paper focuses on 3GPP-like GBSM THz channel modeling based on channel measurements. We first present channel measurements at 100 GHz in an indoor office scenario and at 132 GHz in an urban microcellular scenario. Subsequently, channel characteristics such as PL, delay spread, angle spread, K-factor, cluster characteristic, cross-correlations, and correlation distance are obtained and analyzed using the measurement data. Additionally, statistical values of the channel characteristics are extracted based on the statistical distribution of 3GPP channel models, which can be used to reconstruct the channel impulse response (CIR). Furthermore, these obtained values are compared with the default values in the 3GPP channel model, revealing discrepancies that indicate the default values cannot accurately characterize the THz channel. For instance, for the case of line-of-sight links in the indoor office, the measured cluster number is 4 while the default value is 15. Finally, the channel capacity at THz frequency band is evaluated by the reconstructed CIRs generated by the GBSM using the measured statistical values and the 3GPP default values. It is observed that the 3GPP default values overestimate the THz channel capacity, equivalent to more than 10 bps/Hz larger at a signal-to-noise ratio of 30 dB. Overall, these findings are helpful in understanding and modeling the THz channel, facilitating the application of THz communication techniques for 6G.

Index Terms—Terahertz, channel measurement, 3GPP-like channel model, GBSM, THz communication system

I. INTRODUCTION

A. Background

IN 2020, the commercialization of fifth-generation (5G) networks has been carried out worldwide. Then, a very wide band is needed to achieve the ultra-reliable transmission

Manuscript received xxx; revised xxx; accepted xxx. Date of publication xxx; data of current version xxx. This work was supported in part by the National Science Fund for Distinguished Young Scholars (No. 61925102), the National Natural Science Foundation of China (Nos. 62201086, 62101069, and 62201087), and BUPT-CMCC Joint Innovation Center. (Corresponding author: Jianhua Zhang.)

Zhaowei Chang, Jianhua Zhang, Pan Tang, Lei Tian, and Ximan Liu are with the State Key Lab of Networking and Switching Technology, Beijing University of Posts and Telecommunications, Beijing 100876, China (e-mail: {changzw12345, jhzhang, tangpan27, tianlbupt, liuxm2020}@bupt.edu.cn). Hao Jiang is with the School of Artificial Intelligence/School of Future Technology, Nanjing University of Information Science and Technology, Nanjing 210044, China; and also with the National Mobile Communications Research Laboratory, Southeast University, Nanjing 210096, China (e-mail: jianghao@nuist.edu.cn).

Guangyi Liu is with China Mobile Research Institute, Beijing 100053, China (e-mail: liuguangyi@chinamobile.com).

to support various critical applications, such as vehicle-to-vehicle (V2V) communications, cloud computing, and smart city, following the development of big data [1], [2], [3]. The International Telecommunication Union (ITU) has already estimated that the number of global mobile subscriptions could reach 13.8 billion in 2025 and 17.1 billion in 2030 [4], [5], [6], [7]. Therefore, Terahertz (THz) communication attracts a great deal of attention due to its wide bandwidth between 0.1 to 10 THz, which supports much high-speed data rates from tens of Gbps to several Tbps [8]. To meet the demand for mobile communication systems [9], [10], the THz spectrum would be considered a reliable frequency band for the sixth-generation (6G) communication system, bridging the gap between mm-Wave and optical frequency ranges [11].

THz channel model plays an important role in the design, evaluation, and optimization of THz communication systems [12]. However, the THz channel characteristic and model have changed compared to millimeter wave (mm-Wave). As the frequency goes up to THz and the wavelength gets smaller, the short wavelength of the THz bands would close to particles in the environment, diffraction is weaker and reflection gradually occupies a dominant situation. Thus, it is crucial to carry out the channel measurements and modeling in the THz band.

B. Related Works

Most investigations about THz communication have been carried out. Surveys on atmospheric loss at THz provides the guidance for the allocation of wireless communication [13]. Besides, THz communication has been applied in many areas, such as communication and sensing [14], unmanned aerial vehicle networks [15], and satellite communications [16].

To evaluate the performance of the THz communication system, a number of measurement campaigns have been conducted in the THz bands for channel modeling recently. The measurement scenarios are mainly divided into short-range scenarios, typical indoor scenarios, and outdoor scenarios. For the short-range scenarios, the measurement is conducted at a straight path within the distance of 5.5 m at 140-150, 180-190, and 210-215 GHz [17]. The path loss exponents (PLE) of around 2.1-2.2 are obtained. Similarly, the authors in [18] carried the measurement within 4 m at 110, 140, and 170 GHz and got the PLE of 1.8-1.9. Besides, the measurements in the small open room at 140, 150, 285 GHz [19] to obtain the PLE, and the value of delay spread (DS), angular spread. For the typical indoor scenarios, the office room, corridor, and lobby are the main measurement and modeling scenarios. For example, the measurement in the office room are conducted

at 142 GHz [20]. Based on the measurement, the PLE, DS and the number of cluster and path are compared between 28, 73, 142 GHz. In [21], more channel characteristics are investigated, i.e., the path loss (PL), DS, angular spread, cluster characteristics, and cross-correlations based on the office room measurement at 140 GHz. The corridor and lobby are measured to extract the value of DS and PL at 300 GHz in [22]. For the outdoor scenarios, for example, the measurement in the street canyon at 145 to 146 GHz is conducted to study the parameters of model for the PL, shadowing, DS, angular characteristic, and multipath component (MPC) power distribution [23]. The channel measurements in the urban microcellular (UMi) scenarios at 159 GHz [24] and 142 GHz [25] are conducted to study the PL, delay-domain, and angle-domain characteristics. In short, the research on measurements of the THz channels are mainly around 140, 150, 300 GHz in typical scenarios. The study of parameters analysis and modeling contains PL, DS, angular characteristic and the categories of characteristic statistical modelings are not sufficient for THz channel modeling.

C. Motivation

The approval of the 6G framework and overall objectives by the ITU Radiocommunication Working Party 5D in June 2023 [26] signifies the official commencement of 6G standardization. Consequently, to facilitate the assessment of THz technology, the development of a geometry-based stochastic model (GBSM) THz channel model, similar to the 3rd Generation Partnership Project (3GPP), is imperative. However, existing studies on the THz channel have predominantly focused on its characteristics rather than catering to the modeling requirements, such as GBSM. Additionally, the THz frequency bands allocated for mobile usage by the ITU, such as the bands below 140 GHz (130-134 GHz), have not been extensively investigated. These factors have motivated us to conduct measurements and develop 3GPP-like parameters modeling for the THz channel. This research aims to bridge the gaps in the terms of frequency bands, scenarios, and parameter modeling of the THz channel, with the ultimate goal of enabling the design, deployment, evaluation, and optimization of THz communication systems.

D. Main Contributions

In this paper, we present two measurement campaigns in typical hotspot scenarios, specifically at 100 GHz in an indoor office and 132 GHz in UMi scenarios. These scenarios include both line of sight (LoS) and non-line of sight (NLoS) conditions. Based on the measurements, we extract and analyze various parameters such as PL, DS, azimuth angle spread of arrival (ASA), K-factor, cluster number, cluster DS, cluster ASA, cluster K-factor, cross-correlations, and correlation distance. The channel characteristics are then statistically modeled based on the statistical distribution of the 3GPP channel model. We compare the measured statistical values with the default values in the 3GPP channel model. Finally, we calculate the channel capacity of the THz communication system using the reconstructed channel impulse responses (CIRs), which are

generated by the channel statistical characteristic parameters from the measurement and the 3GPP channel model. The contributions of this paper are as follows:

- We conduct two extensive channel measurement campaigns at 100 GHz in the indoor office scenario and at 132 GHz in the UMi scenario. For the measurement at 100 GHz, a total of 19080 (54 rotation angles \times 18 measurement points \times 20 snapshots) CIRs are collected. For the measurement at 132 GHz, the total 907200 (108 RX rotation angles \times 7 TX rotation angles \times 24 measurement points \times 50 snapshots) CIRs are collected.
- Based on the measurement, we extract and analyze the channel characteristics, i.e., the PL, DS, ASA, K-factor, cluster number, cluster DS, cluster ASA, cluster K-factor, cross-correlations, and correlation distance. Then, the statistical values of the channel characteristics are extracted and summarized according to the statistical distribution of the 3GPP channel model. These obtained values can be used in the channel model standardization. Furthermore, the channel statistical characteristics are compared to the 3GPP channel model and between scenarios (LoS-NLoS and the indoor office-the UMi).
- The channel capacity is calculated using the CIRs obtained from the GBSM, which utilizes the measured statistical characteristic parameters and the default values from the 3GPP channel model. By comparing the capacities obtained from both methods, it is observed that the 3GPP default values lead to an overestimation of the THz channel capacity.

The remainder of the paper is organized as follows. Section II provides an introduction to the setup of the channel sounder, the measurement environment, and the measurement procedures. Section III covers the data processing, calculation of channel characteristics, and the implementation of the GBSM. Section IV analyzes the channel characteristics, extracts statistical parameters, and compares the measured results with the default values in the 3GPP channel model. Section V presents the implementation framework of the 3GPP-like THz GBSM and simulates the channel capacity to evaluate the performance of the THz communication system. Finally, Section VI presents the conclusion of this paper.

II. TERAHERTZ CHANNEL MEASUREMENTS

The channel model forms the cornerstone of the technology research and system trial [27]. Conducting wireless propagation channel measurements [28] is the most direct and effective way to obtain these channel models, as measurements can account for greater variability in environments compared to simulation. In this paper, channel measurements are conducted using a channel sounder for the indoor office scenario at 100 GHz, which represents the upper boundary of the current 3GPP working frequency band. Additionally, measurements are conducted for the UMi scenario at 132 GHz, which are the unexplored frequency points within the bands (130-134 GHz) allocated by the ITU for mobile use [29]. The measurement setup, procedures, and data processing will be introduced in the following section. The measurement setup, procedures, and data processing will be introduced in the following part.

TABLE I
THE CHANNEL SOUNDER SETUP.

Parameter	Value of Office	Value of UMi
Tx height	1.8 m	11.6 m
Rx height	1.5 m	1.5 m
Centre frequency	100 GHz	132 GHz
Bandwidth	1.2 GHz	1.2 GHz
Sampling rate	1.5 GHz	1.2 GHz
Sequence samples	511	511
Sequence duration	0.85 μ s	0.85 μ s
IF frequency	4 GHz	6 GHz
LO frequency	12 GHz	21 GHz
Multiplying factor	8	6
Antenna gain at TX	8 dBi	22.5 dBi
Antenna gain at RX	19.7 dBi	24.5 dBi
Horizontal/vertical HPBW at TX	60°/60°	14°/12°
Horizontal/vertical HPBW at RX	20°/15°	10°/9°
Antenna polarization at TX	Circular	Vertical
Antenna polarization at RX	Vertical	Vertical
Azimuth rotation range at RX	[0°, 360°)	[0°, 360°)
Elevation rotation range at RX	[-15°, 15°]	[-9°, 9°]
Azimuth rotation step	20°	10°
Elevation rotation step	15°	9°

A. Channel sounder setup

At the transmitter (TX) side, a vector signal generator (R&S SMW 200A) generates the intermediate frequency (IF) signal. The signal is a modulated signal using amplitude shift keying (ASK) from a periodic 511 samples Pseudo-Noise 9 (PN9) sequence with a duration of 0.85 μ s. The signal propagates through the cable and multiplies a local oscillator (LO) signal generated by the signal generator (R&S SMB 100A) using the frequency multiplier. Thus, the IF signal is mixed with the LO signal and multiplied to the THz bands. A horn antenna with high gain is used to transfer the THz signal. At the receiver (RX) side, a horn antenna is used to receive the THz signal. Then, the THz signal is down-converted by a frequency mixer and becomes the IF signal. A spectrum analyzer (R&S FSW 43) catches the IF signal and demodulates it. The CIRs are obtained after the data processing by the laptop. The channel platform is shown in Fig. 1.

For the measurement at 100 GHz, the frequency multiplying factor is 8. The IF and LO frequencies are 4 and 12 GHz, respectively. At the RX side, 1278 in-phase and quadrature (IQ) signal samples are obtained with a sample rate of 1.5 GHz. TX and RX antenna gains are 8 and 19.7 dBi respectively. Half power beam width (HPBW) at TX and RX in the horizontal plane are 60° and 20°, and in the vertical plane is 60° and 15°, respectively. The circular polarization antenna at TX provides wide beamwidth but reduces about 3 dBi gain due to the vertical polarization reception.

For the measurement at 132 GHz, the frequency multiplying factor of the frequency multiplier is 6. The IF and LO frequencies are 6 and 21 GHz, respectively. Besides, 1022 IQ signal samples are obtained with a sample rate of 1.2

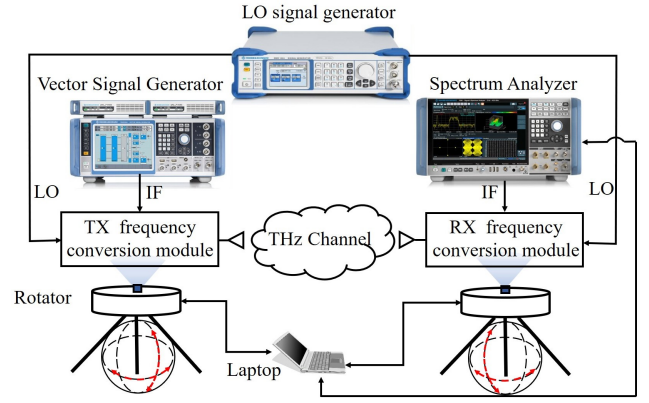


Fig. 1. The structure of channel sounding platform.

GHz. The lower sample rate is used in the large scenario to reduce the sampling time under the premise of sufficient delay resolution. The antenna gains at TX and RX are 22.5 and 24.5 dBi, respectively. The HPBWs of the Tx antenna are 14° and 12° for horizontal and elevation planes. The HPBWs of RX antenna for horizontal and elevation plane are 10° and 9°. The details of the channel sounder configuration for the measurement campaigns are shown in Table I.

B. Measurement environment and procedures

For the measurement at 100 GHz, the channel measurement is conducted in an indoor office room with an area of 17.51 \times 6.78 m². The office contains open cubicle area, walled office, open area, and corridor etc. Fig. 2(a) illustrates the measurement layout for both LoS and NLoS cases. The measurement environment in the indoor office is shown in Fig. 2(b). The top of Fig. 2(a) displays the locations of the TX and RX in the LoS case. The LoS locations distribute in the open cubicle areas and open areas. The RXs in the LoS case are also affected by the walled office between the TX_{1I}. Besides, TX_{2I} in the corridor radiates to the office area to investigate the case that TX/RX is interfered by the corridor walls. The distribution of TX and RX is representative for the indoor office scenario and covers the definition of the 3GPP. In detail, TX_{1I} serves ten RX locations, namely RX_{1IL} to RX_{10IL} with corresponding distances of 4.5, 3.2, 2.7, 6.3, 5.7, 5.5, 8.5, 8.3, 10.4, and 10.1 m, respectively. For each TX-RX in the LoS case, one TX best-pointing elevation angle that maximizes the received power at RX is set and three elevation angles are used at RX, i.e., the RX best-pointing elevation angle, and the RX antenna uptilts and down-tilts by 15° from the RX best-pointing elevation angle. For each TX and RX elevation angle combination, the TX best-pointing azimuth angle is set and the RX antenna is rotated 360° in the azimuth plane with a step of 20° to catch all the possible multi-paths in any azimuth directions. All steps of the rotation are selected to one HPBW of the corresponding antennas. Below Fig. 2(a) are the measurement locations in the NLoS case. TX_{2I} serves eight RX locations, namely RX_{1IN} to RX_{8IN}, with distances of 14.2, 14.0, 11.2, 10.9, 8.6, 8.1, 5.5, and 4.2 m, respectively. For each TX-RX in the NLoS

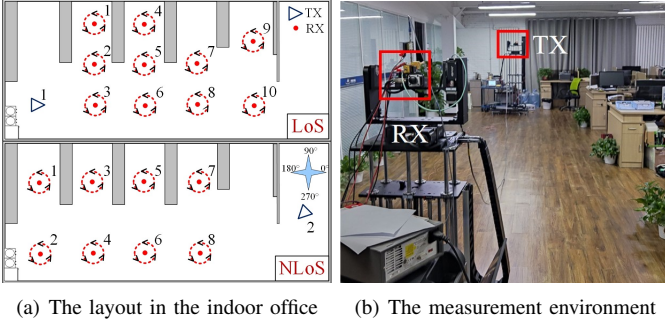


Fig. 2. The measurement layout (a) and the measurement environment (b) in the office office.

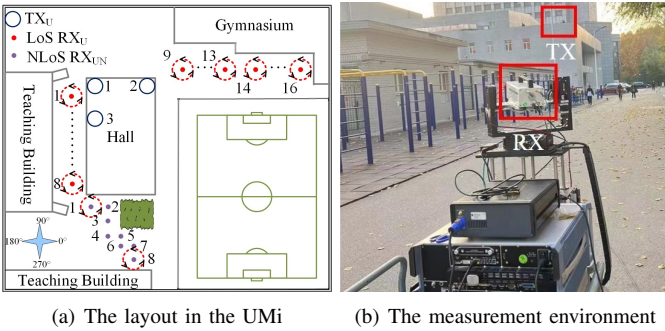


Fig. 3. The measurement layout (a) and the measurement environment (b) in the UMi.

case, the horizontal angle is used at TX and three elevation angles are used at RX, i.e., the horizontal angle, and the RX antennas up-tilt and down-tilt by 15° from the horizontal angle. TX radiates towards the wall at a 45° incident angle in the azimuth plane. The RX azimuth plane rotation in the NLoS case follows the same approach as in the LoS case. In the measurement for each TX-RX elevation and azimuth angle combination, 20 snapshots of IQ data were collected. For the measurement at 132 GHz, the UMi scenario and locations of measurement points of channel measurement are illustrated in Fig. 3(a). The measurement environment in the UMi is shown in Fig. 3(b). TX is set at TX_{1U} and TX_{2U} for LoS case and set at TX_{3U} for NLoS case. The TX and RX heights are maintained at 11.6 and 1.5 m, respectively, throughout the measurement. Also, 24 locations of RX (RX_{1UL}-RX_{16UL}) in the LoS case and RX (RX_{1UN}-RX_{8UN}) are set at a total of three routes as shown in Fig. 2(b). RX_{1UL}-RX_{8UL} are set to investigate the street canyon area, and RX_{9UL}-RX_{16UL} are represent the urban open area. RX_{1UN}-RX_{8UN} are blocked by the body of the hall, and can be utilize to study the NLoS case. The set of TX and RX is typical for the UMi scenario. The distances between TX_{1U} and RX_{UL} for LoS measurements are as follows: RX_{1UL} - 14.2 m, RX_{2UL} - 17.5 m, RX_{3UL} - 21.6 m, RX_{4UL} - 25.9 m, RX_{5UL} - 30.5 m, RX_{6UL} - 35.1 m, RX_{7UL} - 39.9 m, and RX_{8UL} - 44.7 m. Besides, for TX_{2U} and RX_{UL}, the distances from RX_{9UL} to RX_{16UL} in the LoS case are 53.9, 58.7, 63.5, 68.4, 73.3, 83.0, 92.8, and 102.7 m, respectively. For each RX_{UL} location in the LoS case, TX_U is aligned with RX at the elevation

angle, and seven azimuth angles are used at TX_U (the aligned angle and rotations of the TX_U antenna by 14 degrees in both clockwise and counterclockwise directions, repeated three times). The distances between TX_{3U} and RX_{UN} from RX_{1UN} to RX_{8UN} in the NLoS case are 56.7, 56.9, 61.8, 67.7, 68.1, 71.4, 71.9, and 76.4 m, respectively. For each RX_{UN} location in the NLoS case, TX_U and RX_{UN} are in the direction of maximum primary reflection. For each TX-RX combination, three elevation angles are utilized at RX (the aligned angle, and the RX antennas up-tilt and down-tilt 9° from the aligned angle), and the RX antenna is rotated 360° in the azimuth plane with a step of 10° to catch all the possible rays in any azimuth directions. In the measurement for each TX-RX elevation and azimuth angle combination, 50 snapshots of IQ data were collected.

III. PROCESSING OF MEASUREMENT

After conducting the measurement described in Section II, the data needs to be processed in order to generate the power delay profile (PDP). The calibration procedure for the system is explained in detail in [27]. This procedure involves removing the system and antenna response from the original data through calibration. Subsequently, the omnidirectional PDP and other channel characteristics can be derived from the directional PDPs. Finally, the channel characteristics can be used to describe the channel transfer function (CTF) using GBSM. This section will cover the synthesis of PDPs, computation of channel characteristics, and the theoretical GBSM.

A. Synthesizing PDPs

The obtained CIRs after the system calibration are directional, representing the channel responses for specific azimuth and elevation angles. The thresholds are selected to be 10 dB above the average noise power (ANP) of PDPs in the indoor office scenario and 6 dB above the ANP of PDPs in the UMi scenario (low noise amplifier with better performance are use for the UMi measurement). In order to get the omnidirectional PDP, we synthesize the directional PDPs by selecting the strongest path among all azimuth and elevation directions for each delay bin:

$$h_{\text{omni}}(\tau) = \max_{\phi_{\text{TX}}, \phi_{\text{RX}}, \theta_{\text{RX}}} h(\tau, \phi_{\text{TX}}, \phi_{\text{RX}}, \theta_{\text{RX}}), \quad (1)$$

where h denotes the directional PDPs, ϕ_{TX} and ϕ_{RX} are the azimuth orientation of TX and RX, respectively, θ_{RX} is the elevation orientation of RX, and τ is per delay bin.

B. Computing channel characteristics

To characterize the THz propagation channel, the computation of the channel characteristics based on the directional and omnidirectional PDP is introduced in this part.

1) *Path loss and shadowing*: PL reflects the influence of the distance between the TX and RX on the quality of the received signal [30]. The omnidirectional and the strongest directional PL is calculated by the negative value of the sum of the power of all the paths on each delay bin:

$$PL_{\text{O}}[\text{dB}] = - \sum_{i=1}^L |h_{\text{omni}}(\tau_i)|^2, \quad (2)$$

$$PL_B[\text{dB}] = -\sum_{i=1}^L |h(\tau_i, \Phi_{\text{RX}}, \Theta_{\text{RX}})|^2, \quad (3)$$

with

$$(\Phi_{\text{RX}}, \Theta_{\text{RX}}) = \arg \max_{\phi_{\text{RX}}, \theta_{\text{RX}}} \sum_{i=1}^L |h(\tau_i, \phi_{\text{RX}}, \theta_{\text{RX}})|^2, \quad (4)$$

where PL_O is the omnidirectional PL, PL_B is the PL of strongest-power direction, τ_i is the i th delay bin, L is the number of delay bins, and Φ_{RX} and Θ_{RX} are the azimuth and elevation angle of the maximum power direction. For modeling the PL as a function of distance, the close-in (CI) model is utilized which can be expressed as:

$$PL_{\text{CI}}(f, d)[\text{dB}] = PL_{\text{FSPL}}(f, d_0) + 10n \log_{10}\left(\frac{d}{d_0}\right) + \epsilon, \quad (5)$$

where f is the center frequency of the radio wave in GHz, d_0 is a physically-based reference distance which is set to 1 m in this paper, n is the PLE, d is the distance between TX and RX, and ϵ is a zero-mean Gaussian variable with a standard derivation σ representing the shadowing, and $PL_{\text{FSPL}}(f, d_0)$ is the free space PL. It is written as:

$$PL_{\text{FSPL}}(f, d_0)[\text{dB}] = 20 \log_{10}\left(\frac{4\pi d_0 f}{c}\right), \quad (6)$$

where c is the speed of light. To obtain the parameters of the CI model, methods such as maximum likelihood estimation (MLE) can be used to fit the measurement results.

2) *RMS DS*: The RMS DS is the second central moment of the PDP and is calculated as:

$$\tau_{\text{rms}} = \sqrt{\frac{\sum_{i=1}^L (\tau_i - \tau_{\text{mean}})^2 |h_{\text{omni}}(\tau_i)|^2}{\sum_{i=1}^L |h_{\text{omni}}(\tau_i)|^2}}, \quad (7)$$

with

$$\tau_{\text{mean}} = \frac{\sum_{i=1}^L \tau_i |h_{\text{omni}}(\tau_i)|^2}{\sum_{i=1}^L |h_{\text{omni}}(\tau_i)|^2}. \quad (8)$$

3) *Angular spread*: The measurement campaign obtains the multi-paths from 360° in the horizontal direction with a step of the HPBW. To explore the dispersion of power over different angular directions, the angular spread should be computed. The first step is synthesizing all elevational PDPs at the same azimuth direction and getting directional angular power (DAP):

$$DAP(\phi_{\text{RX}}) = \max_{\phi_{\text{TX}}, \theta_{\text{RX}}} \sum_{\tau} |h(\tau, \phi_{\text{TX}}, \phi_{\text{RX}}, \theta_{\text{RX}})|^2. \quad (9)$$

Then, ASA can be computed by DAP as:

$$ASA = \sqrt{\frac{\sum_{\phi_{\text{RX}}} |e^{j\phi_{\text{RX}}} - ASA_{\text{mean}}|^2 DAP(\phi_{\text{RX}})}{\sum_{\phi_{\text{RX}}} DAP(\phi_{\text{RX}})}}, \quad (10)$$

where j is the imaginary unit, and the average ASA ASA_{mean} is written as:

$$ASA_{\text{mean}} = \frac{\sum_{\phi_{\text{RX}}} e^{j\phi_{\text{RX}}} DAP(\phi_{\text{RX}})}{\sum_{\phi_{\text{RX}}} DAP(\phi_{\text{RX}})}. \quad (11)$$

4) *K-factor*: It is important to analyze the distribution of the MPC over the delay domain [31]. The K-factor K_R is defined as the ratio of the strongest MPC to other MPCs in the LoS case:

$$K_R = \frac{\max_{\tau} |h_{\text{omni}}(\tau)|^2}{\sum_{\tau} |h_{\text{omni}}(\tau)|^2 - \max_{\tau} |h_{\text{omni}}(\tau)|^2}. \quad (12)$$

C. The principle of the 3GPP GBSM

The 3GPP GBSM is introduced to describe the CTF in the THz channel in this subsection, which has the advantage of characterizing the characteristics of randomly distributed scatterers by the fundamental laws of electromagnetic wave reflection, diffraction, and scattering. The 3GPP GBSM models the rays by the three-dimensional (3D) pattern of the antennas, the arrival, and departure angles to characterize the geometric feature of the channel. The CIF of the whole multiple-input multiple-output (MIMO) channel $\mathbf{H}(\tau, t)$ can be described by $M_t \times M_r$, where M_t and M_r are the number of elements at the TX and RX sides, respectively. The element of the matrix presented by the GBSM means the CTF for s th TX element and u th RX element and can be written as [32]:

$$h_{u,s}(\tau, t) = \sqrt{\frac{1}{K_R + 1}} h_{u,s}^{\text{NLoS}}(\tau, t) + \sqrt{\frac{K_R}{K_R + 1}} h_{u,s}^{\text{LoS}}(t) \delta(\tau - \tau^{\text{LoS}}), \quad (13)$$

where $h_{u,s}^{\text{NLoS}}(\tau, t)$ is the CTF of clusters at the case of NLoS, $h_{u,s}^{\text{LoS}}(t)$ is the CTF of the LoS clusters, $\delta(\cdot)$ is the Dirac's delta function, and τ^{LoS} is the delay of the LoS cluster. Besides, τ_n denotes the delay of the n th cluster. $h_{u,s}^{\text{NLoS}}(\tau, t)$ can be expressed as [32]:

$$h_{u,s}^{\text{NLoS}}(\tau, t) = \sum_{n=1}^2 \sum_{i=1}^3 \sum_{m \in R_i} h_{u,s,n,m}^{\text{NLoS}}(t) \delta(\tau - \tau_{n,i}) + \sum_{n=3}^N h_{u,s,n}^{\text{NLoS}}(t) \delta(\tau - \tau_n), \quad (14)$$

where n is the cluster number, N is the total cluster number, m is the rays in the cluster, R_i is the mapping to rays at sub-cluster i , $\tau_{n,i}$ is the delay of rays of sub-cluster i at cluster n . The rays of the two strongest clusters ($n = 1$ and 2) are spread to delay to three sub-clusters (per cluster), with fixed delay offset. The mapping to rays R_1 , R_2 , and R_3 are $\{1, 2, 3, 4, 5, 6, 7, 8, 19, 20\}$, $\{9, 10, 11, 12, 17, 18\}$, and $\{13, 14, 15, 16\}$, respectively.

The delays of the sub-clusters $\tau_{n,1}$, $\tau_{n,2}$, and $\tau_{n,3}$ are τ_n , $\tau_n + 1.28C_{\text{DS}}$, and $\tau_n + 2.56C_{\text{DS}}$ with $C_{\text{DS}} = 3.91$ ns, respectively. The CTF of the cluster n $h_{u,s,n}^{\text{NLoS}}(t)$ is written as Eq. (15), where

- $[\cdot]^T$ is the transposition of the matrix.
- M is the number of the total rays in a cluster.
- P_n denotes the power of the cluster n .
- $F_{\text{rx},u,\theta}$, $F_{\text{rx},u,\phi}$, $F_{\text{tx},s,\theta}$, $F_{\text{tx},s,\phi}$ denote the radiation pattern of elements u at RX of the vertical and horizontal polarization and elements s at TX of the vertical and horizontal polarization, respectively. Besides, θ represents

$$h_{u,s,n}^{\text{NLoS}}(t) = \sum_{m=1}^M h_{u,s,n,m}^{\text{NLoS}}(t) = \sqrt{\frac{P_n}{M}} \sum_{m=1}^M \begin{bmatrix} F_{\text{rx},u,\theta}(\theta_{n,m,\text{ZoA}}, \phi_{n,m,\text{AoA}}) \\ F_{\text{rx},u,\phi}(\theta_{n,m,\text{ZoA}}, \phi_{n,m,\text{AoA}}) \end{bmatrix}^T \begin{bmatrix} e^{j\Phi_{n,m}^{\theta\theta}} & \sqrt{\kappa_{n,m}^{-1}} e^{j\Phi_{n,m}^{\theta\phi}} \\ \sqrt{\kappa_{n,m}^{-1}} e^{j\Phi_{n,m}^{\phi\theta}} & e^{j\Phi_{n,m}^{\phi\phi}} \end{bmatrix} \begin{bmatrix} F_{\text{tx},s,\theta}(\theta_{n,m,\text{ZoD}}, \phi_{n,m,\text{AoD}}) \\ F_{\text{tx},s,\phi}(\theta_{n,m,\text{ZoD}}, \phi_{n,m,\text{AoD}}) \end{bmatrix} e^{j2\pi(\mathbf{r}_{\text{rx},n,m} \cdot \mathbf{d}_{\text{rx},u})/\lambda_0} e^{j2\pi(\mathbf{r}_{\text{tx},n,m} \cdot \mathbf{d}_{\text{tx},s})/\lambda_0} e^{j2\pi(\mathbf{r}_{\text{rx},n,m} \cdot \mathbf{v})t/\lambda_0} \quad (15)$$

the vertical polarization and ϕ represents the horizontal polarization.

- $\theta_{n,m,\text{ZoA}}$, $\phi_{n,m,\text{AoA}}$, $\theta_{n,m,\text{ZoD}}$, and $\phi_{n,m,\text{AoD}}$ are the zenith angle of arrival (ZoA), the azimuth angle of arrival (AoA), the zenith angle of departure (ZoD), and the azimuth angle of departure (AoD) of the m th ray in n th cluster.
- $\Phi_{n,m}^{\theta\theta}$, $\Phi_{n,m}^{\theta\phi}$, $\Phi_{n,m}^{\phi\theta}$, and $\Phi_{n,m}^{\phi\phi}$ are the random phase for four different polarization combinations ($\theta\theta$, $\theta\phi$, $\phi\theta$, $\phi\phi$) of the m th ray in n th cluster. Besides, $\kappa_{n,m}$ is the cross-polarization power ratio (XPR) of the m th ray in the n th cluster.
- $\mathbf{r}_{\text{rx},n,m}$ and $\mathbf{r}_{\text{tx},n,m}$ denotes the spherical unit vector at RX with $\theta_{n,m,\text{ZoA}}$ and $\phi_{n,m,\text{AoA}}$ and at TX with $\theta_{n,m,\text{ZoD}}$ and $\phi_{n,m,\text{AoD}}$, respectively. For example, $\mathbf{r}_{\text{rx},n,m}$ is given by:

$$\begin{bmatrix} \sin \theta_{n,m,\text{ZoA}} \cos \phi_{n,m,\text{AoA}} \\ \sin \theta_{n,m,\text{ZoA}} \sin \phi_{n,m,\text{AoA}} \\ \cos \theta_{n,m,\text{ZoA}} \end{bmatrix}^T. \quad (16)$$

- $\mathbf{d}_{\text{rx},u}$ and $\mathbf{d}_{\text{tx},s}$ denotes the location vector of receive antenna element u and transmit antenna element s .
- $\frac{\mathbf{r}_{\text{rx},n,m} \cdot \mathbf{v}}{\lambda_0}$ is the Doppler frequency component. λ_0 is the wavelength of the carrier frequency. The \mathbf{v} is written as:

$$\mathbf{v} = v \cdot [\sin \theta_v \cos \phi_v \quad \sin \theta_v \sin \phi_v \quad \cos \theta_v]^T, \quad (17)$$

where v is the user velocity vector, θ_v is the travel elevation angle, and ϕ_v is the travel azimuth angle.

In the LoS case, the $h_{u,s}^{\text{LoS}}(t)\delta(\tau - \tau^{\text{LoS}})$ can be expressed as Eq. (18), where $-2\pi\frac{d}{\lambda_0}$ is the initial phase for both $\theta\theta$ and $\phi\phi$ polarization of the LoS link.

The THz channel exhibits distinct characteristics due to the unique properties of THz waves, such as their short wavelength. For instance, the composition of clusters, which serves as the fundamental unit in the GBSM, may undergo changes. Therefore, it becomes necessary to extract various types of the THz channel parameters:

- The spread parameters, cross-correlations, and correlation distance of the spread parameters are utilized to generate correlated large-scale parameters, namely DS, angle spread (AS), shadow fading, and K-factor. The large-scale parameters are represented by the lognormal distribution, as described in [32]. The small-scale parameters (delay, AoA, AoD, ZoA, ZoD) in the GBSM are computed based on the correlated large-scale parameters.
- The power of the path is calculated by the PL and K-factor. The PL is modeled by the CI model.
- The cluster parameters such as the cluster number, number of rays per cluster, in-cluster DS, and in-cluster AS

are utilized to divide the MPCs into clusters to describe the CTF of the channel.

The next section will analyze and model the PL and spread parameters based on the channel characteristics computation introduced in Section III-B. Additionally, the cluster parameters, cross-correlations, and correlation distance of the spread parameters will be presented.

IV. MEASUREMENT RESULT

In this section, channel characteristics are extracted, and analyzed. They are then compared with the 3GPP channel statistical characteristics parameters [32]. Finally, the corresponding parameters for meeting the requirements of the GBSM at the indoor office and the UMi scenario will be summarized.

A. PDPs

Fig. 4a-Fig. 4b shows some positions of PDPs in the indoor office in this section, with the biggest MPC aligned at the TX-RX distance. The LoS measurement is taken at a distance of 10.1 m. Fig. 4a presents the omnidirectional and best-directional PDPs in the LoS case. The LoS path is observed in both the omnidirectional and best-directional PDPs. The second strongest MPC is 9 dB lower than the LoS path. Besides, there are subsequent MPCs following the LoS MPC, which are not observed in the best-directional PDP. For the NLoS case, the position with a distance of 10.9 m is shown in Fig.4b. Apart from the biggest first reflection MPC, multiple MPCs carry power levels up to 24 dB lower than the LoS path and only can be seen in omnidirectional PDP. Moreover, the NLoS case exhibits a richer multipath environment compared to LoS case.

Fig. 4c-Fig. 4d presents the PDP at RX8_{UL} and RX8_{UN} in the UMi. Similarly, the LoS MPC in the LoS case or the biggest first reflection MPC in the NLoS case exists at both omnidirectional and best-directional PDPs. In the case of RX8_{UL}, as shown in Fig. 4c, the omnidirectional PDP reveals multiple MPCs occurring after 100 ns, with their powers being at least 27 dB lower than the LoS MPC. Compared to the indoor office, the expansive UMi scenario provides a larger channel space, leading to the generation of more MPCs with farther propagation distances in the LoS case. For the RX8_{UN} PDP presented in Fig. 4d, the number of MPCs is fewer compared to the NLoS case in the indoor office and even lower than the MPCs observed at RX8_{UL}. That is because the location of the RX and the TX in the UMi scenario in the NLoS case makes it more challenging for RX to receive THz waves with reflection as the main way of propagation.

$$h_{u,s}^{LoS}(t) = \begin{bmatrix} F_{rx,u,\theta}(\theta_{LoS,ZoA}, \phi_{LoS,AoA}) \\ F_{rx,u,\phi}(\theta_{LoS,ZoA}, \phi_{LoS,AoA}) \end{bmatrix}^T \begin{bmatrix} 1 & 0 \\ 0 & -1 \end{bmatrix} \begin{bmatrix} F_{tx,s,\theta}(\theta_{LoS,ZoD}, \phi_{LoS,AoD}) \\ F_{tx,s,\phi}(\theta_{LoS,ZoD}, \phi_{LoS,AoD}) \end{bmatrix} e^{-j2\pi \frac{d}{\lambda_0}} e^{\frac{j2\pi(\mathbf{r}_{rx,LoS} \cdot \mathbf{d}_{rx,u})}{\lambda_0}} e^{\frac{j2\pi(\mathbf{r}_{rx,LoS} \cdot \mathbf{v})t}{\lambda_0}} \quad (18)$$

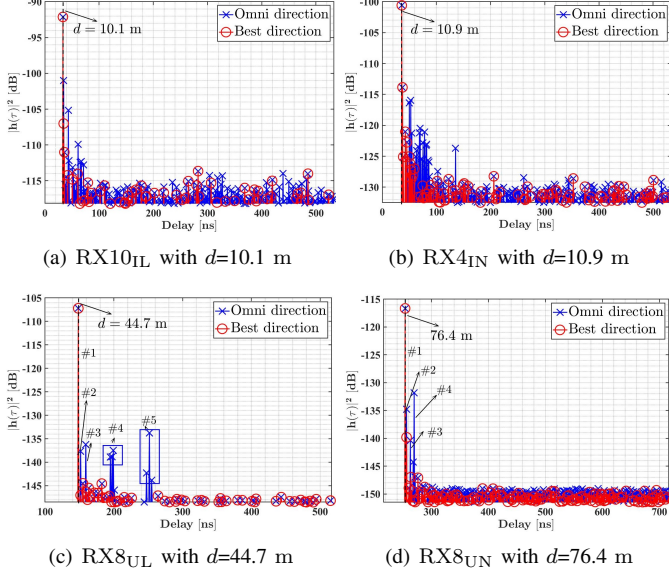


Fig. 4. PDP for two positions (RX10_{IL} and RX4_{IN}) in the indoor office and two positions (RX8_{UL} and RX8_{UN}) in the UMi at LoS and NLoS cases, respectively

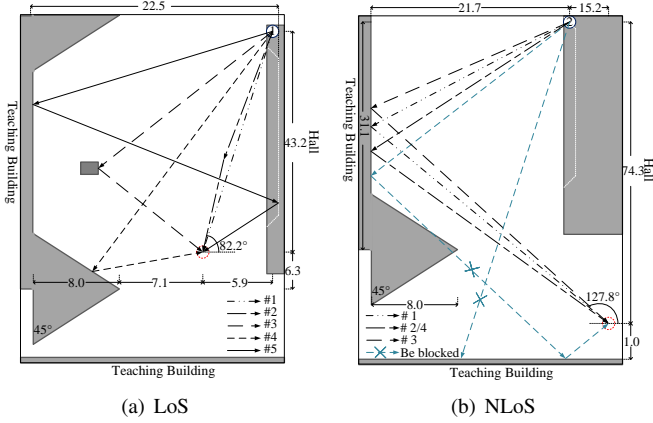


Fig. 5. The propagation path analysis in the RX8_{UL} and RX8_{UN} (the unit of distance is m).

Fig. 5 shows the propagation path deduced according to the AoA, ZoA, and the Δd , which is the difference in propagation distance to the first arrival path, to analyze and explore the fewer clusters or MPCs in the two PDPs in the UMi. The AoA, ZoA, and Δd are listed in Table II. For the LoS case, cluster 1 is the LoS path, and cluster 2 is from the direction of the LoS path with the ZoA = 4.2° and the Δd = 1 m which is reflected from the ground. It is worth mentioning that the HPBW of 9° in elevation allows the RX with the ZoA = 4.2° to be capable of receiving MPCs with the ZoA < 0°. The calculated AoA of cluster 1 and cluster 2 is 82.2°. It is within the scope of the

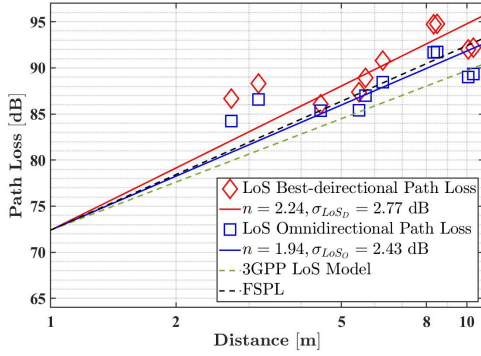
TABLE II
CLUSTER INFORMATION OF RX8_{UL} AND RX8_{UN}.

Cluster number	RX8 _{UL}			RX8 _{UN}		
	AoA (°)	ZoA (°)	Δd (m)	AoA (°)	ZoA (°)	Δd (m)
#1	85.2	13.2	0.0	124.2	8.0	0.0
#2	85.2	4.2	1.0	134.2	8.0	0.8
#3	145.2	4.2	3.3	114.2	8.0	2.8
#4	195.2	13.2	14.0-15.3	134.2	8.0	4.8
#5	45.2	4.2	29.8-32.0	-	-	-

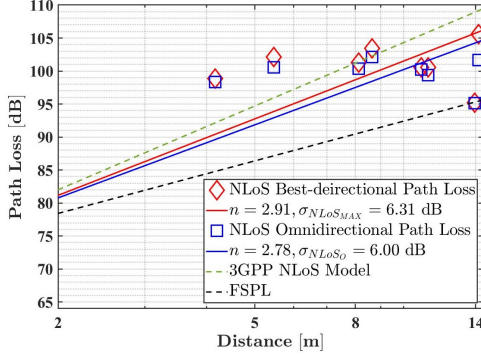
RX HPBW with the actual received AoA = 85.2° (85.2° ± 5°). Cluster 3 is received in the direction of 60° away from the LoS path with the Δd = 3.3 m. The calculated horizontal distance from the RX to the reflector for cluster 3 is 6.2 m. The reflector at this location is a row of parked cars which is at the horizontal distance of 4.5-8 m. Cluster 4 is reflected by the projecting part of the teaching building with the AoA = 195.2°. The AoA of the cluster 5 is 45.2°. The calculated propagation distance is 67.2 m which is short by around 7 m compared to the actual measurement in the case of only two specular reflections occurring. It means that the concave glass windows provide longer propagation distance and more reflection ways, for example, scattering.

For the NLoS case, the clusters 1, 2, 3, and 4 are all from the direction near the maximum reflection path and the difference in propagation distance is within 4.8 m. Similar to the LoS path shown in Fig. 5, the calculated AoA of cluster 1 is 127.8° and is also within the scope of the RX HPBW. The uneven surface of the teaching building and the large HPBW of RX and TX leads to more accessible paths around the first reflection path. However, the location of the TX and RX, and the environment prevent the RX from receiving additional AoA of MPCs. Take two cases for example. First, the teaching building at the bottom of Fig. 5b, another reflector for the two-order path, reflects the path to the left space and Rx can not receive it. Second, the three-order path reflected by both teaching buildings is blocked by the projecting part of the left teaching building. That is because the horizontal distance (8 m) from the top of the projecting part to the flat surface of the left teaching building is larger than the horizontal distance from the path to the flat surface of the left teaching building which is computed as 2.6 m. Overall, RX in the NLoS case is harder to receive the MPCs with different AoA and DS compared to RX in the LoS case in this UMi scenario.

Based on the PDPs, additional investigation and modeling of other channel characteristics will be carried out for the THz GBSM in the subsequent subsections. The statistical value of the channel characteristics, calculated in a manner similar to



(a) LoS in the indoor office



(b) NLoS in the indoor office

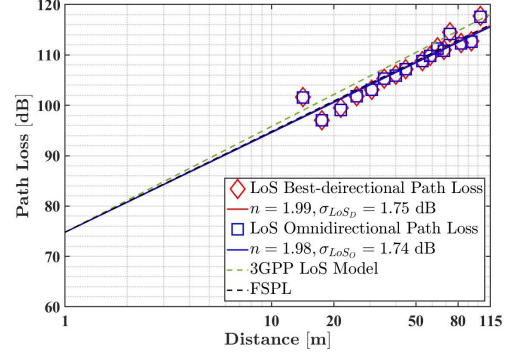
Fig. 6. PL at LoS and NLoS cases for the indoor office.

the 3GPP standard, are summarized in Table III.

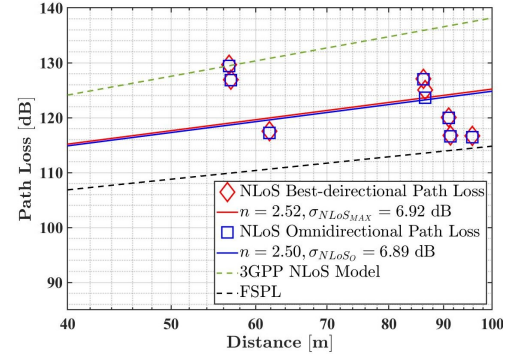
B. Path loss and shadowing

1) *Analysis of the indoor office at 100 GHz:* Fig. 6a shows the best-directional and omnidirectional PL results in the LoS case, the FSPL model, and the 3GPP PL model with PLE of $n = 1.73$ and SF standard deviation of $\sigma = 3$ dB at 100 GHz [32] for the indoor office. The omnidirectional PLE is $n = 1.94$ with the SF standard deviation of $\sigma = 2.43$ dB, which is slightly smaller than the PLE $n = 2.24$ at the best direction in the LoS case. It indicates that MPCs power can be captured from directions other than boresight-aligned direction. The similar phenomenon can be observed at 142 GHz [25]. The omnidirectional PL is higher than the 3GPP PL model in the LoS case because the MPCs in THz channel are fewer than those in the 3GPP.

Fig. 6b presents the best-directional and omnidirectional PL results in the NLoS case, the FSPL model, and the 3GPP PL model with $n = 3.19$ and $\sigma = 8.29$ dB at 100 GHz [32] for the NLoS case. The omnidirectional PLE is $n = 2.78$ with the SF standard deviation of $\sigma = 6.00$ dB, which is smaller than but close to the PLE of $n = 2.91$ in the best direction. This finding indicates that the best-directional power typically dominates among all MPCs. The omnidirectional PL is lower than the PL model of the 3GPP in the NLoS case. This is because the more MPCs in the 3GPP result in additional scattering, diffraction, and obstacle-blocking losses. For specific points of the PL results, it is worth mentioning that the PL of RX2_{IN} ($d = 14.0$ m) in the NLoS case is



(a) LoS in the UMi



(b) NLoS in the UMi

Fig. 7. PL at LoS and NLoS cases for the UMi.

close to the free space PL. This phenomenon can be attributed to the significant incident angle of the best-directional rays reflecting from TX to RX, resulting in minimal reflection and propagation losses, and the propagation distance of the path being close to the TX-RX distance d . A similar observation was made in the street canyon measurement at 145 GHz [33]. The results of $n = 1.8$ and $\sigma = 2.9$ dB in the LoS case, as well as $n = 2.7$ and $\sigma = 6.6$ dB in the NLoS case, are presented for comparison in the NYU WIRELESS research center [20]. Our results align with the parameters. Furthermore, many of the RX positions in the NYU measurement are located in the corridor, allowing for more captured reflection paths due to the waveguide effect. This ultimately leads to a smaller PLE.

2) *Analysis of the UMi scenario at 132 GHz:* Fig. 7a-Fig. 7b shows the best-directional and omnidirectional PL results at LoS and NLoS cases, and the FSPL model for the UMi scenario. For comparison, the 3GPP PL model with $n = 2.1$ and $\sigma = 4$ dB in the LoS case is shown in Fig. 7a. Besides, Fig. 7b presents the 3GPP PL model in the NLoS case at 132 GHz [32]. The model is written as:

$$PL(d)[dB] = 67.57 + 35.5 \times \log_{10}(d). \quad (19)$$

The observation of the small deviation value of 0.01 between the PLEs of best-directional and omnidirectional model means that the received direction of the best direction contains the most power and a lot of energy other MPCs is lost due to the long propagation distance. For the comparison between the measurement and the 3GPP channel model, the measured PL is smaller, indicating that fewer MPCs with more power

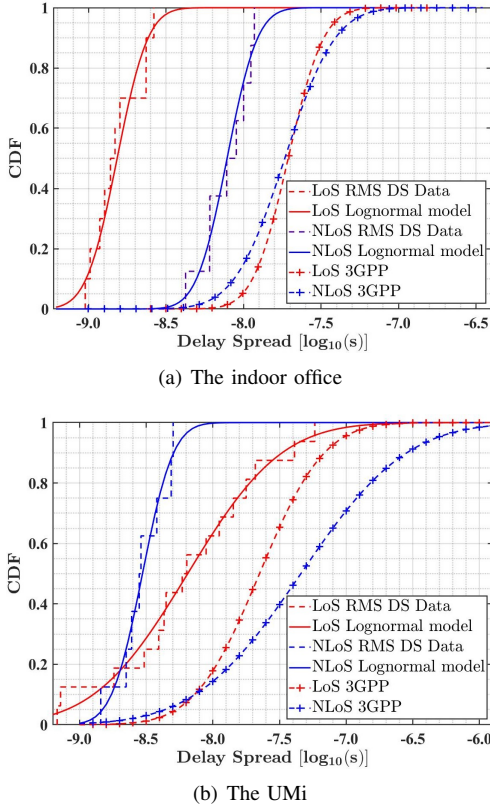


Fig. 8. Normal distribution modeling of RMS DS at LoS and NLoS cases for two scenarios.

in the THz channels avoid more consumption in the large-distance transmission scenario. The path losses of RX7_{UN} and RX8_{UN} positions in the NLoS case close to the FSPL, which is consistent with the findings in the indoor office scenario. Besides, the PL tends to decrease with the increase of distance, because a larger incidence angle with distance causes a smaller reflection loss [34], which is also observed in [35]. This indicates that reflection, particularly the first reflection, is the primary propagation mechanism in the THz channel for both indoor and outdoor NLoS scenarios. Besides, the larger shadowing fading of 2.43 dB is observed in the indoor office in the LoS case than it is in the UMi. It indicates that the indoor office produces more enriched reflection paths than the UMi. The similar results of the PLEs in the LoS case are $n = 1.94$ and $n = 1.9$ measured in the NYU [25] and USC [35], respectively. However, the NLoS PLEs among the NYU, USC and our measurement are discrepant. The NYU presents a higher PL with $n = 2.87$, and the USC discusses a PL of up to 15 dB higher than the FSPL model which is closer to our works due to the similarity of the scenario with RXs distributed in “street canyon”.

C. Delay characteristics

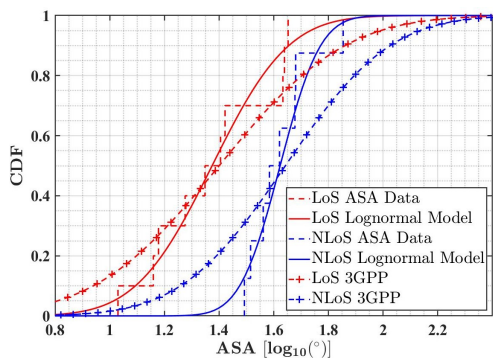
Fig. 8a presents the cumulative density function (CDF) of the measurement and 3GPP RMS DS in the indoor office. The RMS DS is plotted on a logarithmic scale, i.e., dBs. The measurement RMS DS for indoor office scenario at LoS τ_{LoS} and NLoS cases τ_{NLoS} follow the lognormal distri-

bution with $\mu = -8.82 \log_{10}(s)$, $\sigma = 0.15 \log_{10}(s)$ and $\mu = -8.11 \log_{10}(s)$, $\sigma = 0.15 \log_{10}(s)$, respectively. RMS DS is $-8.81 \log_{10}(s)$ and $-8.10 \log_{10}(s)$ at 50% cumulative probability of LoS and NLoS cases, respectively. Notably, the RMS DS in the NLoS case is significantly larger than that in the LoS case, indicating greater spatial dispersion in NLoS cases. The 3GPP RMS DS for the indoor office scenario at LoS and NLoS cases follow the lognormal distribution with $\mu = -7.71 \log_{10}(s)$, $\sigma = 0.18 \log_{10}(s)$ and $\mu = -7.73 \log_{10}(s)$, $\sigma = 0.26 \log_{10}(s)$, respectively [32]. The measured RMS DS of LoS and NLoS cases is smaller than that of the 3GPP channel model which suggests the MPCs at the THz channel have shorter propagation distances. That means the THz channel would lose many long-distance MPCs that exist in the low-frequency channel and become sparser. The NYU presents -8.52 and $-8.04 \log_{10}(s)$ as the mean value of RMS DS in the LoS case and NLoS case [20], respectively. These values are a little bigger than the measurement results, as the NYU measures a larger office.

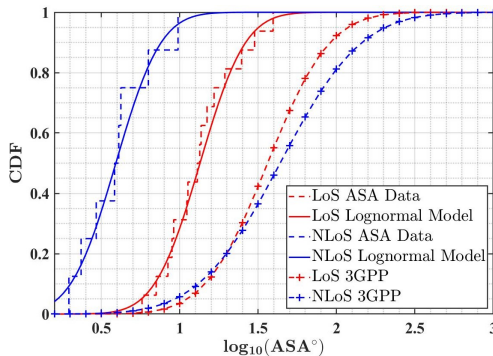
Fig. 8b shows the CDF of the UMi. The measurement RMS DS at LoS τ_{LoS}^U and NLoS τ_{NLoS}^U cases follow the lognormal with $\mu = -8.19 \log_{10}(s)$, $\sigma = 0.55 \log_{10}(s)$ and $\mu = -8.53 \log_{10}(s)$, $\sigma = 0.18 \log_{10}(s)$, respectively. The RMS DS in the NLoS case is smaller than in the LoS case. It indicates that the MPCs in the NLoS case are less than in the LoS case, which can be also observed in Fig. 4c-Fig. 4d. The presence of open space around the RX in NLoS cases results in fewer reflectors, thus reducing the number of MPCs. These results align well with those in [35], which obtains a small RMS DS in the NLoS case, and it is even reach to LoS results. The The 3GPP RMS DS for the UMi scenario at LoS and NLoS cases follow the lognormal distribution with $\mu = -7.65 \log_{10}(s)$, $\sigma = 0.38 \log_{10}(s)$ and $\mu = -7.34 \log_{10}(s)$, $\sigma = 0.62 \log_{10}(s)$, respectively [32]. This suggests that the THz channel exhibits sparser MPCs than the low-frequency channel, which is consistent across both the indoor office and UMi scenarios.

D. Azimuth angular characteristics

Fig. 9a shows the ASA results of the measurement and the 3GPP at 100 GHz. The measured ASA at LoS and NLoS cases in the indoor office follow the lognormal distribution with $\mu = 1.37 \log_{10}(^\circ)$, $\sigma = 0.21 \log_{10}(^\circ)$ and $\mu = 1.62 \log_{10}(^\circ)$, $\sigma = 0.11 \log_{10}(^\circ)$, respectively. The 50% cumulative probability of ASA is $1.31 \log_{10}(^\circ)$ and $1.61 \log_{10}(^\circ)$, respectively. The NLoS channel has more MPCs from multiple angles, so NLoS case has a larger ASA than LoS case. Besides, the 3GPP ASA at LoS and NLoS cases follow the lognormal distribution with $\mu = 1.40 \log_{10}(^\circ)$, $\sigma = 0.36 \log_{10}(^\circ)$ and $\mu = 1.64 \log_{10}(^\circ)$, $\sigma = 0.30 \log_{10}(^\circ)$, respectively. Compared to the 3GPP channel model, the measured ASA exhibits a higher concentration around the average value. This can be attributed to the fact that THz propagation primarily occurs through reflection, while the millimeter wave (mm-wave) channel, as defined by 3GPP, involves multiple propagation mechanisms such as reflection, transmission, and diffraction. Consequently, the THz channel experiences fewer receiving



(a) The indoor office

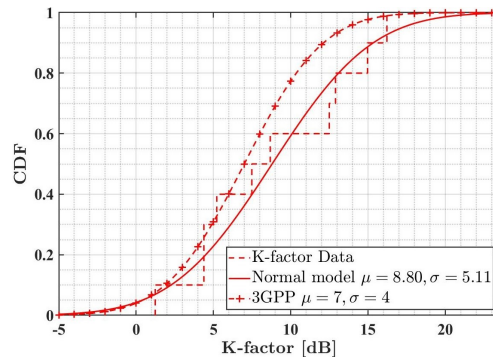


(b) The UMi

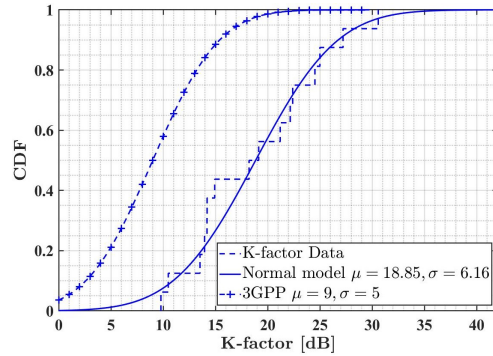
Fig. 9. Normal distribution Modeling of ASA at LoS and NLoS cases for two scenarios.

angles of MPCs and a lower occurrence of ASA compared to the mm-Wave channel. In [21], the similarity values of ASA are 1.46 and 1.69 $\log_{10}(\circ)$ for LoS and NLoS case, respectively. Furthermore, [20] reveals a smaller ASA, with the mean ASA in the NLoS case being 0.73 $\log_{10}(\circ)$ and smaller than that in the LoS case, attributed to the specific RX setup mentioned in subsection IV-B.

Fig. 9b shows the ASA results of the measurement and the 3GPP at 132 GHz. The measurement ASA at LoS and NLoS cases in the UMi follow the lognormal distribution with $\mu = 1.13 \log_{10}(\circ)$, $\sigma = 0.23 \log_{10}(\circ)$ and $\mu = 0.59 \log_{10}(\circ)$, $\sigma = 0.23 \log_{10}(\circ)$, respectively. The ASA in the NLoS case is smaller than that in the LoS case. That is because the RX in the NLoS channel only receives the MPCs around the first reflection direction. The major power of the THz channel in the UMi is received from a narrow arrival angle as shown in Fig. 5b. A lot of paths after the first reflection are reflected in the large space and can not arrive at the RX according to the geometric theory. This phenomenon have also been observed in [20] and [35]. The mean ASAs in [35] are even less than 0 $\log_{10}(\circ)$ at LoS and NLoS case. The 3GPP ASA at LoS and NLoS cases follow the lognormal distribution with $\mu = 1.56 \log_{10}(\circ)$, $\sigma = 0.31 \log_{10}(\circ)$, and $\mu = 1.64 \log_{10}(\circ)$, $\sigma = 0.41 \log_{10}(\circ)$, respectively. The huge difference between the ASA of the measurement and the 3GPP channel model indicates that the reflection dominating propagation at THz makes it hard to receive MPCs in the UMi.



(a) The indoor office



(b) The UMi

Fig. 10. Modeling for K-factor for two scenarios.

E. K-factor

In this subsection, the K-factor of the measurement and 3GPP for two scenarios are analyzed in Fig. 10. Fig. 10a shows the K-factor of the measurement and 3GPP [32] in the indoor office in dB, which follow the normal distribution with $\mu = 8.80$ dB, $\sigma = 5.11$ dB and $\mu = 7$ dB, $\sigma = 4$ dB, respectively. The measured K-factor is bigger than that of the 3GPP because the THz channel has fewer MPCs, and the power of LoS path dominates among all MPCs.

The modeling results of the measurement in the UMi are presented in Fig. 10b. Similarly, the measured K-factor in dB in the UMi with the normal distribution of $\mu = 18.85$ dB, $\sigma = 6.16$ dB is bigger than the default values in the 3GPP channel model with the normal distribution of $\mu = 9$ dB, $\sigma = 5$ dB. Besides, the K-factor in the UMi is larger than that in the indoor office. The reason is that the MPCs in the UMi with the long propagation distance have smaller power than those in the indoor office. Thus, the power in the UMi is more focused on the dominant path.

F. Cluster characteristics

The cluster is the basic unit that constitutes the channel space-time propagation characteristics. We employ the K-power-means algorithm to cluster the MPCs, with cluster centroids iteratively adjusted based on the multiple component distance (MCD) [36]. The statistical results for cluster mean numbers, cluster DS, cluster ASA, and cluster K-factor are calculated and shown in Table III.

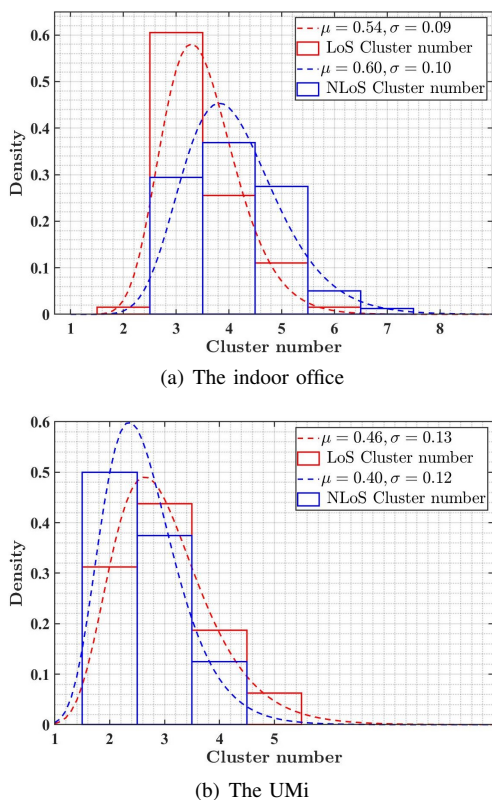


Fig. 11. The PDF of cluster numbers for two scenarios.

For the indoor office, the DS and ASA in the LoS case are smaller compared to NLoS case, indicating that the MPCs within a cluster exhibit greater similarity in terms of delay and angle. The cluster numbers in the LoS case are less than it in the NLoS case. Fig. 11a shows the results of statistical fitting for the cluster numbers in the indoor office at LoS and NLoS cases. Furthermore, the cluster numbers follows lognormal distribution with $\mu = 0.54$, $\sigma = 0.09$ and $\mu = 0.60$, $\sigma = 0.10$ at LoS and NLoS cases, respectively. The cluster numbers of the same scenario are similar and present a smaller-variance lognormal distribution which is different from the traditional Poisson model at mm-wave [37]. The reason is that reflection dominates the THz propagation mechanism and the small indoor office scenario provides a simple reflector layout. Fig. 12a-12b illustrate the clustering results at RX10_{IL} in the LoS case and RX6_{IN} in the NLoS case, respectively. The first arriving path is set at 0 ns. The clusters in the LoS case are almost from two angles. These two angles differ by 60° while the clusters in the NLoS case are from about three directions involving 180°. The NLoS case has more MPCs and the signal can cover more directions. Besides, it is found that more than one cluster is in similar angular intervals. That is because the wide beamwidth of TX creates large-scale MPCs with different propagation distances to be reflected.

For the UMi, the DS, ASA, and cluster numbers in the LoS case are bigger, which indicates that the street canyon provides more MPCs with different long propagation distances in the LoS case. Besides, it is difficult to generate paths with abundant AoAs and distances in the NLoS case in the UMi.

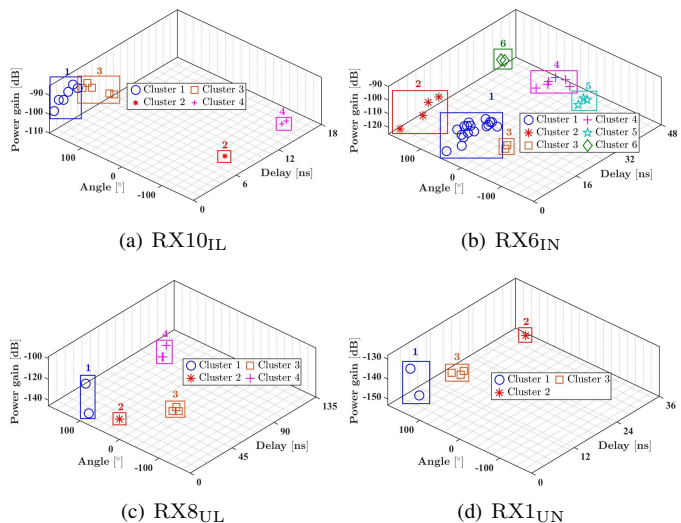


Fig. 12. The clustering result at RX10_{IL} and RX6_{IN} in the indoor office and at RX8_{UL} and RX1_{UN} in the UMi.

It is found that the DS is bigger than that in the indoor office in the LoS case. That is because the propagation distance of MPCs is longer in the UMi. Furthermore, the cluster numbers follows lognormal distribution with $\mu = 0.46$, $\sigma = 0.13$ and $\mu = 0.40$, $\sigma = 0.12$ at LoS and NLoS cases, respectively. The clustering results at RX8_{UL} in the LoS case and RX1_{UN} in the NLoS case are shown in Fig. 12c-12d. The first arriving path is set at 0 ns. The reflection clusters in the LoS case contain three clusters (clusters 2, 3, and 4) at the AoA of 60°, 110° and 40° away from the LoS clusters, respectively, while almost all clusters are at AoA around the first-reflection directions in the NLoS case. The farthest spreading clusters are approximately 100 ns (equivalent to 30 m) in the LoS case and 30 ns (equivalent to 9 m) in the NLoS case away from the nearest spreading cluster. The clusters in the NLoS case are all reflected by the uneven surface of the left teaching building.

G. Cross-Correlations and correlation distance in the horizontal plane

The cross-correlations and The correlation distance in the horizontal plane of both scenarios are summarized in Table III. For the indoor office, ASA shows a positive correlation with DS at both LoS and NLoS case. This can be attributed to the dispersion of the channel in the angular domain, which is likely to be correlated with dispersion in the delay domain. The ASA and DS exhibit a positive correlation with SF in the LoS case, whereas they are negatively correlated with SF in the NLoS case. This is because SF means more reflection disperses the channel energy at both LoS and NLoS cases, but in the NLoS case, the MPCs are harder to be received. The DS is negatively correlated with the K-factor since a small K-factor means a weaker dominant LoS path and a more dispersive channel. The ASA does not show a correlation with the K-factor, indicating that the angular dispersion of MPCs in the office is sufficiently large and is not easily affected by the MPCs power. The SF is negatively correlated to the K-factor

TABLE III
THE 3GPP-LIKE CHANNEL PARAMETERS OF THE MEASUREMENT.

Scenarios		Office LoS	Office NLoS	UMi LoS	UMi NLoS
PL (CI model)	PLE	1.94	2.78	1.98	2.50
lg DS= \log_{10} (DS/1s)	$\mu_{\text{lg DS}}$	-8.82	-8.11	-8.19	-8.53
	$\sigma_{\text{lg DS}}$	0.15	0.15	0.55	0.18
lg ASA= \log_{10} (ASA/1°)	$\mu_{\text{lg ASA}}$	1.37	1.62	1.13	0.59
	$\sigma_{\text{lg ASA}}$	0.21	0.11	0.23	0.23
SF [dB]	σ_{SF}	2.43	6.00	1.74	6.89
K [dB]	μ_K	8.80	-	18.85	-
	σ_K	5.11	-	6.16	-
Cross-Correlations	ASA vs DS	0.10	0.33	0.45	-0.42
	ASA vs SF	0.38	-0.57	-0.30	0.10
	DS vs SF	0.47	-0.49	-0.10	0.56
	DS vs K	-0.32	-	-0.66	-
	ASA vs K	0.05	-	-0.10	-
	SF vs K	0.67	-	-0.20	-
Number of clusters		4	5	3	3
Number of rays per cluster		3	5	3	2
Cluster DS (C_{DS}) in [ns]		0.5	1.4	4.1	0.3
Cluster ASA (C_{ASA}) in [°]		1.5	4.7	0.8	0.6
Cluster K-factor (C_K) in [dB]		1.47	-1.43	13.49	10.88
Correlation distance in the horizontal plane [m]	ASA	2.1	2.4	5.6	3.1
	DS	1.9	1.0	4.9	4.7
	SF	2	0.8	5.2	7.8
	K	2.4	-	2.5	-

because a larger SF causes the attenuation of the MPCs power, resulting in the dominant LoS path having a larger proportion.

The correlation distance in the horizontal plane is shown in Table III. For the indoor office, the correlation distance presents the maximum distance at which parameters of two location points are kept relevant. The correlation distance of DS and SF in the LoS case is larger than that in the NLoS case, which means DS and SF are more stationary over the distance in the LoS case. The correlation distance of ASA in the LoS case are smaller than that in the NLoS case, which indicates the MPCs propagating in a small and closed room (NLoS) exhibit greater spatial consistency in the angular domain.

For the UMi, the ASA and DS are positively correlated in the LoS case because both ASA and DS represent the dispersion of MPCs. Analogously, the ASA and DS are negatively correlated with the K-factor due to a small K-factor means the dominant LoS path is weaker and thus the channel is more dispersive. ASA and DS are negatively correlated in the NLoS case because a large DS means a long propagation distance and low MPCs power. Thus, the MPCs scattered next to the first reflection direction have lower power, causing the power to be more concentrated in the first reflection direction. ASA and DS have a positive correlation with SF in the NLoS case. The larger SF in the NLoS case means more reflection, and MPCs with different DS and AoA. Besides, DS and ASA have a negative correlation with SF in the LoS case because more SF results in less power for MPCs. SF is negatively corrected to the K-factor because larger SF causes more MPCs

by reflection and more MPCs can be received by the RX, thus the LoS path has a smaller proportion. Besides, it is found that the correlations between DS and SF, and between SF and K-factor for both two scenarios are quite different. The reason is that SF in the indoor office means attenuation of the power for all the MPCs while SF in the UMi means more reflections and MPCs have more chances to be received.

For the correlation distance in the UMi, the correlation distance of ASA and DS in the LoS case is larger than that in the NLoS case, indicating that these parameters exhibit greater spatial stationarity over the distance in the LoS case. In contrast, as a case with primary reflection as the main mode of propagation, the NLoS case has less variation in SF with distance. Besides, the correlation distance in the UMi is larger than that in the indoor office due to the wider range of distances present in the UMi scenario.

V. CHANNEL CAPACITY SIMULATION

In this section, we investigate the THz 3GPP-like 3D GBSM framework and compare the channel capacity of THz communication systems in both the indoor office and UMi scenarios. THz communication systems are intended to be used at the base station (BS) to support high-speed data rates of Gbps for mobile users (MUs). To analyze the impact of frequency on channel capacity and compare the performance calculated using measured statistical values with the default values in the 3GPP channel model, we evaluate the single-user channel capacity at THz for two scenarios. The simulation is

TABLE IV
PARAMETERS OF COMMUNICATION SYSTEM SIMULATION.

Scenario	Indoor office	UMi
Carrier frequency	100 GHz	132 GHz
BS height	3 m	10 m
MUs height	1.5 m	1.5 m
Bandwidth	1 GHz	1 GHz
BS transmit power	20 dBm	40 dBm
BS antenna gain	5 dBi	5 dBi
MUs antenna gain	5 dBi	5 dBi

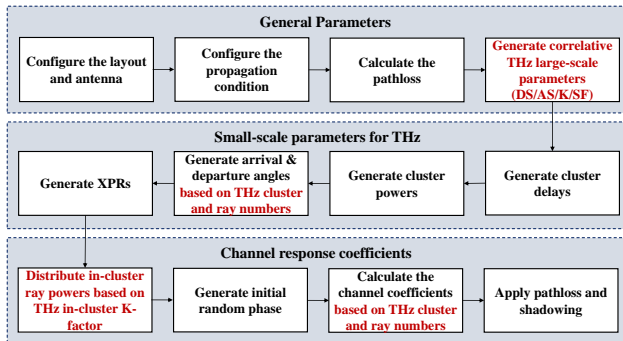


Fig. 13. THz 3GPP-like GBSM implementation framework.

conducted using the GBSM [32] and a simulation software [38], following a step-by-step approach. The THz GBSM simulation framework is an extension of the current 3GPP GBSM framework, as shown in Fig. 13.

Based on the channel modeling procedure in 3GPP [32], the extended framework includes several modifications and additional steps. These include generating THz large-scale parameters based on Table. III, generating arrival and departure angles based on the THz large-scale parameters, distributing in-cluster ray powers by THz in-cluster K-factor introduced in [39], and calculating the channel coefficients based on the cluster and ray numbers at THz. The in-cluster K-factors in the indoor office at 100 GHz and in the UMi at 132 GHz are shown in Table III. It is worth noting that the measurement results for cluster number, cluster DS, and cluster ASA are much smaller than those in the 3GPP model, making the set of sub-clusters to compensate for delay offset is unnecessary. The NLoS GBSM at THz can be simplified to [32]:

$$h_{u,s}^{\text{TN}}(\tau, t) = \sum_{n=1}^N h_{u,s,n}^{\text{NLoS}}(t) \delta(\tau - \tau_n). \quad (20)$$

The simulated communication links are operating at 100 GHz in the indoor office and 132 GHz in the UMi scenario with 16×16 omnidirectional antennas BS and 2×2 omnidirectional antennas MUs. The numbers of BS and MUs antenna refer to [37]. The details of parameters are shown in Table IV. The channel capacity defined as maximal achievable transmission rate is calculated by:

$$C = \log_2 \det[\mathbf{I}_{M_r} + \frac{\rho}{M_t} \mathbf{H}(\tau, t) \mathbf{H}^H(\tau, t)], \quad (21)$$

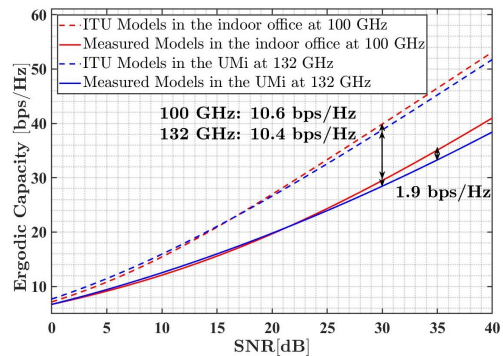


Fig. 14. The channel capacity for measurement and 3GPP model at 100 GHz in the indoor office and at 132 GHz in the UMi.

where M_r and M_t are the numbers of MUs and BS antenna, which are 4 and 256, respectively. Besides, \det presents computing the value of the determinant of the matrix, \mathbf{I}_{M_r} is a unit matrix with the dimension of $M_r \times M_r$, ρ is the mean SNR, $\mathbf{H}(\tau, t)$ is the $M_r \times M_t$ MIMO channel matrix which is the simulation result, and superscript H represents the conjugate transpose of a matrix. Fig. 14 presents the channel capacity obtained by the 3GPP Indoor Hotspot scenario model at 100 GHz [32], 3GPP UMi scenario model at 132 GHz, and obtained 100 GHz and 132 GHz channel parameters. The parameters not obtained by the measurement at 100 GHz and 132 GHz are substituted with corresponding 3GPP parameters. Besides, the outdoor to indoor probability is set to 0 in both scenarios. When the SNR exceeds 21.6 dB, the channel capacity evaluated by the measurement model in the indoor scenario is greater than that in the UMi scenario (equivalent to a 1.9 bps/hz gain at the SNR of 35 dB). The is because the number of clusters in the UMi scenario is lower than that in the indoor office for both LoS and NLoS cases. Furthermore, it has been observed that the 3GPP model predicts higher performance when compared to the measured parameters models, both for the 100 GHz frequency band in the indoor office and the 132 GHz frequency band in the UMi scenario (equivalent to a 10.6 bps/Hz gain at 100 GHz in the indoor office and a 10.4 bps/Hz gain at 132 GHz in the UMi at the SNR of 30 dB). This is because the 3GPP model assumes a greater number of clusters (e.g., at 100 GHz, the 3GPP model predicted 15 clusters while 4 clusters were measured in the indoor-hotspot scenario in the LoS case) and the THz 3GPP-like GBSM takes into account the sparsity of the channel by redistributing the power of the in-cluster rays. Thus, in order to obtain better system performance, it is crucial to leverage the large bandwidth characteristics of THz in the design of THz communication systems.

VI. CONCLUSION

This paper focuses on the 3GPP-like GBSM THz channel modeling based on the measurements at 100 GHz in the indoor office and at 132 GHz in the UMi scenario. Then, the 3GPP-like channel statistical characteristic parameters are extracted, analyzed, and compared with the default values in the 3GPP channel model [32]. Through the analysis of the values, we

find that the UMi exhibits a sparser MPC structure compared to the indoor office scenario. Specifically, the ASA for LoS and NLoS cases in the UMi is $1.13 \log_{10}(\circ)$ and $0.59 \log_{10}(\circ)$, respectively, which is much smaller than $1.37 \log_{10}(\circ)$ and $1.62 \log_{10}(\circ)$ in the office scenario. Besides, it is observed that the cluster numbers are 4 in the indoor office and 3 in the UMi in the LoS case, which are less than those in the 3GPP of 15 and 12, respectively. It means that the THz channel is more sparse and the existing channel models are unavailable to characterize the sparsity above 100 GHz. Furthermore, a large-scale parameters table is presented and these parameters can be used in the channel model standardization for 6G. Finally, the channel capacity of the THz channel is evaluated by the CIRs, which are generated by the GBSM [32] based on the channel characteristic parameters of the measurement and the 3GPP channel model. The default parameters in the 3GPP channel model lead to an overestimated capacity (equivalent to more than 10 bps/Hz larger at the signal-to-noise ratio of 30 dB). Overall, this work contributes to the modeling of the THz channels, the standardization of the THz channel models for 6G, and provides insights for the design and optimization of future 6G communication systems.

As future work, there are two directions: i) Conduct additional measurements for both scenarios, particularly for the NLoS case, to validate the model in terms of data volume; ii) Investigate the impact of various environmental factors on the THz NLoS channel, such as buildings and echo reflector.

REFERENCES

- [1] J. Zhang, J. Lin, P. Tang *et al.*, "Channel measurement, modeling, and simulation for 6G: A survey and tutorial," *arXiv preprint arXiv:2305.16616*, 2023.
- [2] G. Liu, N. Li, J. Deng *et al.*, "The solids 6G mobile network architecture: Driving forces, features, and functional topology," *Engineering-prc*, vol. 8, pp. 42–59, 2022.
- [3] S. Mumtaz, J. M. Jornet, J. Aulin *et al.*, "Terahertz communication for vehicular networks," *IEEE Trans. Veh. Technol.*, vol. 66, no. 7, 2017.
- [4] J. Zhang, J. Lin, P. Tang *et al.*, "Deterministic ray tracing: A promising approach to THz channel modeling in 6G deployment scenarios," *IEEE Commun. Mag.*, 2023.
- [5] J. Zhang, P. Tang, L. Yu *et al.*, "Channel measurements and models for 6G: current status and future outlook," *Front. Inform. Tech. El.*, vol. 21, no. 1, pp. 39–61, 2020.
- [6] J. Zhang, Y. Zhang, Y. Yu *et al.*, "3-D mimo: How much does it meet our expectations observed from channel measurements?" *IEEE J. Sel. Area. Comm.*, vol. 35, no. 8, pp. 1887–1903, 2017.
- [7] J. Zhang, Z. Zheng, Y. Zhang *et al.*, "3D MIMO for 5G NR: Several observations from 32 to massive 256 antennas based on channel measurement," *IEEE Commun. Mag.*, vol. 56, no. 3, pp. 62–70, 2018.
- [8] J. Kokkonen, J. M. Jornet, V. Petrov *et al.*, "Channel modeling and performance analysis of airplane-satellite terahertz band communications," *IEEE Trans. Veh. Technol.*, vol. 70, no. 3, pp. 2047–2061, 2021.
- [9] M. Shafi, J. Zhang, H. Tataria *et al.*, "Microwave vs. millimeter-wave propagation channels: Key differences and impact on 5G cellular systems," *IEEE Commun. Mag.*, vol. 56, no. 12, pp. 14–20, 2018.
- [10] Z. Yuan, J. Zhang, Y. Ji *et al.*, "Spatial non-stationary near-field channel modeling and validation for massive MIMO systems," *IEEE Trans. Antenn. Propag.*, vol. 71, no. 1, pp. 921–933, 2023.
- [11] N. Stepanov, D. Moltchanov, V. Begishev *et al.*, "Statistical analysis and modeling of user micromobility for THz cellular communications," *IEEE Trans. Veh. Technol.*, vol. 71, no. 1, pp. 725–738, 2022.
- [12] T. Jiang, J. Zhang, M. Shafi *et al.*, "The comparative study of s-v model between 3.5 and 28 ghz in indoor and outdoor scenarios," *IEEE Trans. Veh. Technol.*, vol. 69, no. 3, pp. 2351–2364, 2020.
- [13] H. Tataria, M. Shafi, A. F. Molisch *et al.*, "6G wireless systems: Vision, requirements, challenges, insights, and opportunities," *P. IEEE*, vol. 109, no. 7, pp. 1166–1199, 2021.
- [14] C. Chaccour, M. N. Soorki, W. Saad *et al.*, "Seven defining features of terahertz (THz) wireless systems: A fellowship of communication and sensing," *IEEE Commun. Surv. Tut.*, vol. 24, no. 2, pp. 967–993, 2022.
- [15] B. Chang, W. Tang, X. Yan *et al.*, "Integrated scheduling of sensing, communication, and control for mmWave/THz communications in cellular connected UAV networks," *IEEE J. Sel. Area. Comm.*, vol. 40, no. 7, pp. 2103–2113, 2022.
- [16] J. Kokkonen, J. M. Jornet, V. Petrov *et al.*, "Channel modeling and performance analysis of airplane-satellite terahertz band communications," *IEEE Trans. Veh. Technol.*, vol. 70, no. 3, pp. 2047–2061, 2021.
- [17] N. A. Abbasi, A. Hariharan, A. M. Nair *et al.*, "Channel measurements and path loss modeling for indoor THz communication," in *Proc. EuCAP*, Copenhagen, Denmark, 2020, pp. 1–5.
- [18] B. D. Beelde, D. Plets, E. Tanghe *et al.*, "Directional sub-THz antenna-channel modelling for indoor scenarios," in *Proc. EuCAP*, Dusseldorf, Germany, 2021, pp. 1–4.
- [19] M. Lotti, M. Caillet, and R. D'Errico, "Multiband sub-THz double angular characterization in indoor scenario," *IEEE Trans. Antenn. Propag.*, vol. 71, no. 2, pp. 1747–1756, 2022.
- [20] S. Ju, Y. Xing, O. Kanhere *et al.*, "Millimeter wave and sub-terahertz spatial statistical channel model for an indoor office building," *IEEE J. Sel. Area. Comm.*, vol. 39, no. 6, pp. 1561–1575, 2021.
- [21] Y. Chen, C. Han, Z. Yu *et al.*, "140 GHz channel measurement and characterization in an office room," in *Proc. IEEE ICC*, London, UK, 2021, pp. 1–6.
- [22] K. Tamesue, S. Nishi, Z. Wen *et al.*, "300 GHz indoor propagation measurement, simulation and characterization," in *Proc. IEEE MAPE*, Chengdu, China, 2022, pp. 380–385.
- [23] N. A. Abbasi, J. L. Gomez, R. Kondaveti *et al.*, "Thz band channel measurements and statistical modeling for urban d2d environments," *IEEE Trans. Wirel. Commun.*, vol. 22, no. 3, pp. 1466–1479, 2023.
- [24] J. Lee, J.-J. Park, K.-W. Kim *et al.*, "159-GHz propagation measurement and analysis in urban microcellular environment for 6G," *IEEE Wirel. Commun. Lett.*, vol. 12, no. 2, pp. 277–281, 2022.
- [25] Y. Xing and T. S. Rappaport, "Propagation measurements and path loss models for sub-THz in urban microcells," in *Proc. IEEE ICC*, Montreal, QC, Canada, 2021, pp. 1–6.
- [26] ITU, "Framework and overall objectives of the future development of imt for 2030 and beyond," 2023.
- [27] P. Tang, J. Zhang, H. Tian *et al.*, "Channel measurement and path loss modeling from 220 GHz to 330 GHz for 6G wireless communications," *China Commun.*, vol. 18, no. 5, pp. 19–32, 2021.
- [28] J. Zhang, P. Tang, L. Tian *et al.*, "6–100 GHz research progress and challenges from a channel perspective for fifth generation (5G) and future wireless communication," *Sci. China Inform. Sci.*, vol. 60, pp. 1–18, 2017.
- [29] T. Kürner, D. M. Mittleman, and T. Nagatsuma, *THz Communications: Paving the Way Towards Wireless Tbps*. Springer, 2022.
- [30] H. Jiang, B. Xiong, H. Zhang *et al.*, "Physics-based 3D end-to-end modeling for double-RIS assisted non-stationary UAV-to-ground communication channels," *IEEE Trans. Commun.*, vol. 71, no. 7, pp. 4247–4261, 2023.
- [31] P. Tang, J. Zhang, A. F. Molisch *et al.*, "Estimation of the k-factor for temporal fading from single-snapshot wideband measurements," *IEEE Trans. Veh. Technol.*, vol. 68, no. 1, pp. 49–63, 2019.
- [32] 3GPP, "3GPP TR 38.901 V14.1.1 technical report: study on channel model for frequency spectrum above 6 GHz (release 14.1.1)," 2017.
- [33] N. A. Abbasi, J. Gomez-Ponce, R. Kondaveti *et al.*, "Double-directional channel measurements for urban THz microcellular communications in a street canyon," in *Proc. IEEE ICC*, Seoul, Korea, 2022, pp. 2876–2881.
- [34] Z. Chang, J. Zhang, P. Tang *et al.*, "Frequency-angle two-dimensional reflection coefficient modeling based on terahertz channel measurement," *Front. Inform. Tech. El.*, vol. 24, no. 4, pp. 626–632, 2023.
- [35] N. A. Abbasi, J. Gomez-Ponce, R. Kondaveti *et al.*, "Thz band channel measurements and statistical modeling for urban microcellular environments," *IEEE Trans. Wirel. Commun.*, pp. 1–1, 2023.
- [36] Z. Huang, R. Zhang, J. Pan *et al.*, "A framework of multipath clustering based on space-transformed fuzzy c-means and data fusion for radio channel modeling," vol. 69, no. 1, 2020, pp. 4–15.
- [37] P. Tang, J. Zhang, M. Shafi *et al.*, "Millimeter wave channel measurements and modelling in an indoor hotspot scenario at 28 GHz," in *Proc. IEEE VTC-Fall*, Chicago, IL, USA, 2018, pp. 1–5.
- [38] BUPT-ARTT, "BUPTCMG-IMT2030 channel simulation platform," <https://hpc.bupt.edu.cn/dataset-public/datasets/8/>, 2023.
- [39] X. Liu, J. Zhang, P. Tang *et al.*, "Channel sparsity variation and model-based analysis on 6, 26, and 132 GHz measurements," *arXiv preprint arXiv:2302.08772*, 2023.